NURBS-Enhanced Finite Element Method for Euler Equations

R. Sevilla
S. Fernández-Méndez
A. Huerta

NURBS-Enhanced Finite Element Method for Euler Equations

R. Sevilla
S. Fernández-Méndez
A. Huerta

NURBS-Enhanced Finite Element Method for Euler equations

R. Sevilla, S. Fernández-Méndez and A. Huerta[*]

Laboratori de Càlcul Numèric (LaCàN), Departament de Matemàtica Aplicada III,

E.T.S. de Ingenieros de Caminos, Canales y Puertos

Universitat Politècnica de Catalunya,

Jordi Girona 1, E-08034 Barcelona, Spain

e-mail: {ruben.sevilla,antonio.huerta,sonia.fernandez}@upc.es, web http://www-lacan.upc.es

SUMMARY

In this work the NURBS-Enhanced Finite Element Method (NEFEM) is combined with a Discontinuous Galerkin (DG) formulation for the numerical solution of the Euler equations of gas dynamics. With the NEFEM approach numerical fluxes along curved boundaries are computed much more accurately due to the exact geometric representation of the computational domain. The proper implementation of the wall boundary condition provides accurate results even with a linear interpolation of the solution. A detailed comparison of the NEFEM in front of isoparametric finite elements (FE) is presented, demonstrating the superiority of the NEFEM approach for both linear and higher order computations. Copyright © 2007 John Wiley & Sons, Ltd.

----

[*]Correspondence to: Laboratori de Càlcul Numèric (LaCàN), E.T.S. Ingenieros de Caminos, Universitat Politècnica de Catalunya, Jordi Girona 1, E-08034 Barcelona, Spain.

KEY WORDS: NURBS; Discontinuous Galerkin; CAD; exact geometry representation; high-order isoparametric elements; Euler equations

1. INTRODUCTION

The importance of the geometrical model in Finite Element (FE) simulations has recently been pointed out by several authors, see [1, 2, 3, 4, 5, 6] to name a few. For instance, in [3] the error induced by the approximation of curvilinear geometries with isoparametric elements is analyzed in the context of Poisson and Maxwell problems. Using an exact mapping for the geometry in the numerical solution of the Maxwell's equations the error is reduced by an order of magnitude.

When a DG formulation is adopted, the importance of the geometrical model is crucial in some applications, such as the numerical solution of the Euler equations of gas dynamics. In [1] the authors demonstrate that using a linear interpolation for the geometry it is not possible to converge to the steady state solution, even if the mesh is drastically refined near the curved boundary. In [2] a detailed study of this problem is presented to conclude that accurate results can only be obtained taking into account the curvature of the domain. More recently, in [5] a new methodology is presented for the computation of the fluxes across curved boundaries but, unfortunately, the proposed method is not conservative.

The importance of the geometrical model in the numerical solution of the compressible Euler equations is not exclusive of DG methods. In [7, 8] the problem is identified in the context of Finite Volume (FV) methods, and more recent advances in this area can be found in [9, 10].

Non-Uniform Rational B-Splines (NURBS, see [11]) are widely used for geometry description

in CAD (Computer Aided Design). This fact has motivated new numerical methodologies considering an exact representation of the computational domain with NURBS, such as the *isogeometric analysis* [4] and the NURBS-Enhanced Finite Element Method (NEFEM) [6]. The *isogeometric analysis* considers the same NURBS basis functions for both the description of the entire geometry and for the approximation of the solution of the boundary value problem. This idea was first introduced in [12] in the context of thin shell analysis. The NURBS-Enhanced Finite Element Method (NEFEM) also considers an exact representation of the domain but it differs from the *isogeometric analysis* in two main points: the geometry is given by the NURBS description of the boundary (i.e. the information usually provided by CAD), and standard FE polynomial interpolation is considered for the approximation of the solution. Thus, in the large majority of the domain —for elements not intersecting the boundary— a standard FE interpolation and numerical integration is used, preserving the computational efficiency of classical FE techniques. Specifically designed piecewise polynomial interpolation and numerical integration is required for those FE along the NURBS boundary. In [6] the NEFEM is applied to the numerical solution of Poisson and electromagnetic scattering problems. In the numerical solution of Poisson problems with high order isoparametric FE, the optimal rate of h-convergence is not achieved and, consequently, the p-convergence is clearly deteriorated. In contrast, using the NEFEM the optimal rate of h-convergence is obtained for any polynomial degree. Moreover, exponential convergence is observed when a p-refinement strategy is considered, see [6] for NEFEM optimal a priori error estimates. In the context of electromagnetic scattering applications the use of the NEFEM reveals an important improvement with respect to classical isoparametric FE. For the same spatial discretization an important reduction of the error is observed, in some cases more than one order of magnitude.

In addition, for a desired precision the NEFEM is also more efficient because it allows to compute the solution with an important save in number of degrees of freedom.

In this paper the NEFEM is presented as a powerful method for the numerical solution of the Euler equations using a DG formulation. Sections 2 and 3 recall the system of Euler equations and its DG discretization. The basic concepts of the NEFEM are recalled in section 4, with special attention to the interpolation and the numerical integration in elements with one curved edge defined by NURBS. Section 5 presents a classical test for inviscid flow methods in order to evaluate the efficiency and accuracy of the NEFEM in front of classical FE. Low and high order interpolations are tested, and a comparison between isoparametric FE and the NEFEM in terms of the entropy error and other aerodynamic quantities of interest is presented, demonstrating the superiority of the NEFEM approach for the simulation of compressible flow problems.

2. EULER EQUATIONS

Euler equations of gas dynamics express the conservation of mass, momentum and energy for a compressible, inviscid and non-conducting fluid. The strong form of these conservation laws, in the absence of external volume forces, can be written in conservative form as

$$\frac{d\boldsymbol{U}}{dt} + \frac{\partial \boldsymbol{F}_k(\boldsymbol{U})}{\partial x_k} = \boldsymbol{0}, \tag{1}$$

where Einstein notation is assumed (that is repeated indices are implicity summed over), $\boldsymbol{U}$ is the vector of conservation variables and $\boldsymbol{F}_k(\boldsymbol{U})$ are the flux vectors for each spatial dimension

x_k, that is

$$
\boldsymbol{U} = \begin{pmatrix} \rho \\ \rho\boldsymbol{v} \\ \rho E \end{pmatrix}, \qquad \boldsymbol{F}_k(\boldsymbol{U}) = \begin{pmatrix} \rho v_k \\ \rho\boldsymbol{v}v_k + \boldsymbol{e}_k p \\ (\rho E + p)v_k \end{pmatrix},
$$

where ρ is the density, $\rho\boldsymbol{v}$ is the momentum, ρE is the total energy per unit volume, $\boldsymbol{e}_k$ is the

unitary vector in the x_k direction, and p is the pressure, see [13] for more details.

An equation of state, relating the internal energy to pressure and density, completes this

system of nonlinear hyperbolic equations. For a perfect polytropic gas the equation of state is

$$
p = (\gamma - 1)\rho\Big(E - \frac{1}{2}\|\boldsymbol{v}\|^2\Big),
$$

where γ is the ratio of the specific heat coefficients (specific heat at constant pressure over

specific heat at constant volume), with value $\gamma = 1.4$ for air.

A usual quantity for postprocess of inviscid flow computations is the Mach number, defined

as

$$
M = \frac{\|\boldsymbol{v}\|}{c},
$$

where $c = \sqrt{\gamma p/\rho}$ is the speed of sound. For a more detailed presentation of the Euler equations

see for instance [14, 15, 16].

Other useful quantities, usual for the evaluation of the accuracy, are the entropy error

$$
\epsilon_{ent} = \frac{p}{p_\infty}\Big(\frac{\rho_\infty}{\rho}\Big)^\gamma - 1,
$$

the pressure loss

$$
p_{loss} = \frac{p}{p_\infty}\left(\frac{1 + 0.5(\gamma - 1)M^2}{1 + 0.5(\gamma - 1)M_\infty^2}\right)^{\frac{\gamma}{\gamma-1}},
$$

and the pressure coefficient

$$
C_p = \frac{p - p_\infty}{0.5\rho_\infty v_\infty^2},
$$

where the subscript ∞ indicates free-stream values, see [2, 5] for more details.

3. DISCONTINUOUS GALERKIN FORMULATION

This section recalls the basic concepts of DG [17] for the solution of the Euler equations in a open bounded domain $\Omega \subset \mathbb{R}^n$. A regular partition in elements $\overline{\Omega} = \bigcup_e \overline{\Omega}_e$ is assumed, and an element by element discontinuos approximation space is considered.

The weak problem for the strong form of the Euler equations (1) is stated for each element Ω_e. By multiplying by a test vector function $\boldsymbol{W}$, integrating over Ω_e and integrating by parts, the following equation is obtained

$$\int_{\Omega_e} \boldsymbol{W} \cdot \frac{d\boldsymbol{U}_e}{dt} \, d\Omega - \int_{\Omega_e} \frac{\partial \boldsymbol{W}}{\partial x_k} \cdot \boldsymbol{F}_k(\boldsymbol{U}_e) \, d\Omega + \int_{\partial\Omega_e} \boldsymbol{W} \cdot \boldsymbol{F}_{n_e}(\boldsymbol{U}_e) \, d\Gamma = 0 \quad \forall \boldsymbol{W},$$

where $\boldsymbol{U}_e$ denotes the restriction of $\boldsymbol{U}$ to the element Ω_e, $\boldsymbol{n}_e$ is the outward unit normal vector on $\partial\Omega_e$, and the normal flux is defined as

$$\boldsymbol{F}_n(\boldsymbol{U}) = \boldsymbol{F}_k(\boldsymbol{U})n_k,$$

with n_k the k-th component of $\boldsymbol{n}$. As usual in DG methods, to take into account the discontinuous nature of the approximation, the normal flux at the boundary of the element is replaced by a numerical flux, $\widehat{\boldsymbol{F}}_{n_e}(\boldsymbol{U}_e, \boldsymbol{U}_e^{out})$, which is evaluated in terms of the solution in the current element Ω_e and the solution at neighboring elements

$$\boldsymbol{U}_e^{out}(\boldsymbol{x}) = \lim_{\varepsilon \to 0^+} \boldsymbol{U}(\boldsymbol{x} + \varepsilon\boldsymbol{n}_e) \quad \text{for } \boldsymbol{x} \in \partial\Omega_e. \tag{2}$$

The resulting DG weak formulation, to be discretized at each element Ω_e, is

$$\int_{\Omega_e} \boldsymbol{W} \cdot \frac{d\boldsymbol{U}_e}{dt} \, d\Omega - \int_{\Omega_e} \frac{\partial \boldsymbol{W}}{\partial x_k} \cdot \boldsymbol{F}_k(\boldsymbol{U}_e) \, d\Omega + \int_{\partial\Omega_e} \boldsymbol{W} \cdot \widehat{\boldsymbol{F}}_{n_e}(\boldsymbol{U}_e, \boldsymbol{U}_e^{out}) \, d\Gamma = 0 \quad \forall \boldsymbol{W}. \tag{3}$$

Some conditions are required for the definition of a numerical flux function: it must be conservative, Lipstchiz and verify some consistency conditions. Some popular flux functions for the numerical solution of the Euler equations are the exact Riemann solver, the Roe solver,

the Lax-Friederichs solver or the Harten-Lax-van Leer (HLLE) solver, see [18]. In this paper all the numerical computations are performed using the approximate Lax-Friederichs flux function described in [19], that is,

$$\widehat{\boldsymbol{F}}_{n_e}(\boldsymbol{U}_e, \boldsymbol{U}_e^{out}) = \frac{1}{2} \left[\boldsymbol{F}_{n_e}(\boldsymbol{U}_e) + \boldsymbol{F}_{n_e}(\boldsymbol{U}_e^{out}) - \alpha(\boldsymbol{U}_e - \boldsymbol{U}_e^{out}) \right],$$ (4)

where α is the largest eigenvalue of the jacobian matrix $\frac{\partial \boldsymbol{F}_{n_e}}{\partial \boldsymbol{U}}$, i.e.

$$\alpha = \max \left\{ \boldsymbol{v}_e \cdot \boldsymbol{n}_e + c_e , \ \boldsymbol{v}_e^{out} \cdot \boldsymbol{n}_e + c_e^{out} \right\}.$$ (5)

Boundary conditions are implemented following the ideas in [20], initially developed in the context of FV methods. Fictitious elements are considered along the boundary, and the value of the solution is set to impose the boundary conditions through the numerical flux. As usual in the solution of Euler equations a characteristic analysis is performed at the boundary to decide the quantities to be prescribed, see for instance [14, 15, 16] or [21] for implementation details.

The DG formulation (3) is discretized in each element, leading to a system of ordinary differential equations

$$\mathbf{M}\frac{d\mathbf{U}}{dt} + \mathbf{R}(\mathbf{U}) = \mathbf{0},$$ (6)

where $\mathbf{U}$ is the vector of nodal values (or approximation coefficients in a more general case), $\mathbf{M}$ is a block diagonal mass matrix and $\mathbf{R}(\mathbf{U})$ is the residual vector. As it is shown in the examples, the spatial discretization may be performed using isoparametric FE and NEFEM, see section 4. In all experiments, the ODE system (6) is advanced in time using the explicit third order Total Variation Diminishing Runge-Kutta (TVD-RK) scheme presented in [22]. Nevertheless, it is worth noting that semi-implicit and implicit time integration schemes seems to be an efficient alternative for steady state computations, see [23, 24]. The stability condition

for the TVD-RK method requires the use of a CFL number less than or equal to $1/(2p+1)$, where p is the degree of the functional approximation, see [25].

As usual for the solution of non-linear hyperbolic equations, the evaluation of the residual $\mathbf{R}(\mathbf{U})$, which involves the flux at the interior of the elements and their boundaries, can be carried out with two non equivalent options: a quadrature-free implementation or a full quadrature version, see [13]. With a quadrature-free implementation the flux at the integration points is interpolated in terms of the flux nodal values, whereas with a full quadrature version the fluxes are evaluated at integration point level, in terms of the solution at each integration point. The use of a quadrature-free implementation leads to an important save in computational cost thanks to the use of elemental matrices, instead of a loop on integration points. Moreover, for triangles with straight sides (or tetrahedras with planar faces) these elemental matrices can be computed, using the jacobian, from matrices previously computed at the reference element, see [26], with an important saving in computational time. However, numerical experiments reveal that the use of the quadrature-free implementation for the numerical solution of the Euler equations suffer from instability problems in the vicinity of stagnation points, see [27] for a detailed explanation. Thus, all the computations presented in this work are obtained with full quadrature implementation.

4. NEFEM FUNDAMENTALS

A domain $\Omega \subset \mathbb{R}^2$ is considered, whose boundary $\partial\Omega$, or a portion of its boundary, is defined by NURBS curves. A NURBS curve is a curve parametrized by a piecewise rational function, whose definition changes at the so called *breakpoints*, see [11] for a detailed definition. In fact, in practical applications CAD manipulators use *trimmed* NURBS, which are defined by a

restriction of the NURBS parametrization to a subspace of the parametric space.

A triangularization of the domain $\overline{\Omega} = \bigcup_e \overline{\Omega}_e$ is also assumed, such that every triangle Ω_e has at most one side, Γ_e, on the NURBS boundary. Figure 1 shows a domain with part of the boundary described by a NURBS circular curve and a valid triangulation for the NEFEM. As
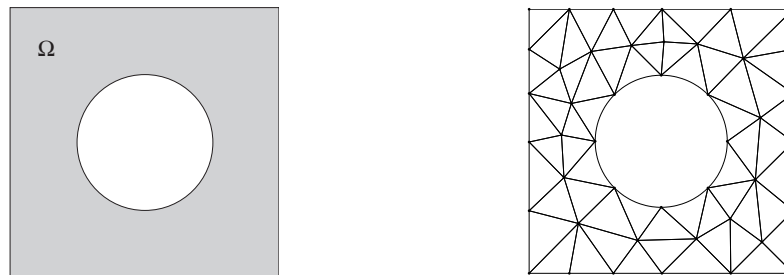

Figure 1. Physical domain with part of the boundary defined by a circular NURBS curve (left) and a valid triangulation for the NEFEM (right)

usual in mesh generation codes, it is also assumed that every curved boundary side belongs to a unique NURBS. That is, a side can not be defined by portions of different NURBS curves, or equivalently, every trimmed NURBS is cut to pieces corresponding to the boundary sides. It is important to note that the breakpoints, which characterize the piecewise nature of NURBS, are independent of the mesh discretization. Thus, the NURBS parametrization can change its definition inside one side, that is break points may belong to element sides and do not need to coincide with FE nodes. This is another major advantage with respect to the isogeometric analysis [4].

For all elements not intersecting the NURBS boundary the usual FE interpolation and numerical integration is considered. The basis of the NEFEM for an element with one side on the NURBS boundary is recalled next.

Let Ω_e be an element with two straight interior sides and one side defined by a trimmed

NURBS, $\Gamma_e = \boldsymbol{C}([\lambda_1^e, \lambda_2^e])$. A *linear transformation* $\boldsymbol{\Psi}$ from local coordinates to physical coordinates is considered, see [6] for details. The linear transformation $\boldsymbol{\Psi}^{-1}$ maps de physic element Ω_e to a curved element $I_e := \boldsymbol{\Psi}^{-1}(\Omega_e)$, see Figure 2. Note that I_e plays the role of the
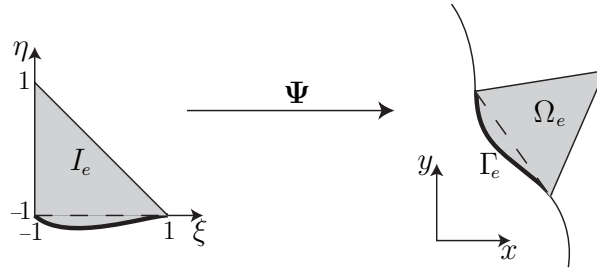

Figure 2. Linear transformation, mapping the curved element $I_e := \boldsymbol{\Psi}^{-1}(\Omega_e)$ to the physic element Ω_e

reference element in standard FE, but here it depends on the definition of its NURBS side. Thus, special numerical strategies are required for every element I_e, see next sections.

Remark 1. *In order to simplify the presentation, it is assumed that the interior vertex of Ω_e is mapped to the vertex $(-1, 1)$ in I_e. The implementation of this condition only requires a proper local numbering of the vertices of the element.*

4.1. FE polynomial basis

In order to work with standard FE polynomial approximations, Lagrange polynomials (that is, standard nodal interpolation) can be considered. In fact, they can be defined on the curved triangle, I_e, in the reference domain or equivalently, in the actual element in the physical domain, Ω_e. The use of a linear transformation from the local (reference) coordinates $\boldsymbol{\xi} = (\xi, \eta)^T$ in I_e to the cartesian coordinates $\boldsymbol{x} = (x, y)^T$ in Ω_e, ensures that a complete polynomial interpolation of degree m in $\boldsymbol{\xi}$ leads to a polynomial interpolation with the same

degree in $\boldsymbol{x}$. Thus, the consistency and accuracy of the approximation is ensured even for elements Ω_e far from being a straight-sided element.

In order to make the computation of the Lagrange polynomials, $\{L_i(\boldsymbol{\xi})\}_{i=1}^{n_{en}}$, more systematic, for any order and for any distribution of nodes, the implementation proposed in [28] is adopted.

Different options can be considered for the definition of a nodal distribution in I_e. For low-order elements equally-spaced nodal distributions can be implemented. Nevertheless, for high-order computations, the use of special distributions of nodes is more convenient in order to reduce the condition number of the resulting elemental matrices, see [29, 30] for details. Fekete points [31] are a good example of such distributions. For curved elements the nodes can be located in the straight-sided triangle given by the vertexs of I_e, see left distribution in Figure 3, or adapted to the exact geometry using the NURBS description, see right distribution in Figure 3. Adapted distributions have a positive influence on the condition number, see [6]. Moreover, numerical experiments reveal that the non-adpated distribution lead to a more restrictive CFL stability condition for the time marching, thus, in the numerical examples adapted distributions are used.
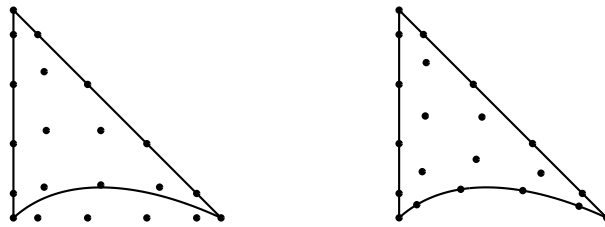

Figure 3. 5th-order nodal distributions in I_e: Fekete points in the straight-side triangle (left) and adapted to the NURBS side (right)

4.2. Numerical integration

The weak form to be solved requires integration along element sides and in the interiors. All the elements not having a side along the NURBS boundary are integrated using standard procedures. The elements with one side, Γ_e, on the NURBS boundary require special attention.

All line integrals to be computed in NEFEM can be written as

$$\int_{\Gamma_e} f \, d\ell = \int_{\lambda_1^e}^{\lambda_2^e} f\big(\boldsymbol{C}(\lambda_i)\big) \, |J_{\boldsymbol{C}}(\lambda)| \, d\lambda,$$

where f is a generic function (polynomial), the side of the element is given by a trimmed NURBS $\Gamma_e = \boldsymbol{C}([\lambda_1^e, \lambda_2^e])$, and $|J_{\boldsymbol{C}}|$ denotes the norm of the differential of the NURBS parametrization $\boldsymbol{C}$ (this is not a polynomial). As usual, a 1D numerical quadrature is used for the numerical computation of the integral, namely

$$\int_{\Gamma_e} f \, d\ell \approx \sum_{i=1}^{\mathbf{n}_{\mathbf{ip}}} f\big(C(\lambda_i)\big) \, |J_{\boldsymbol{C}}(\lambda_i)| \, \omega_i, \tag{7}$$

where λ_i and ω_i are, respectively, the coordinates and weights of the $\mathbf{n}_{\mathbf{ip}}$ integration points in $[\lambda_1^e, \lambda_2^e]$. Recall that the parametrization of a trimmed NURBS, $\boldsymbol{C}$, is a piecewise rational function whose definition changes at breakpoints. Thus, an independent numerical quadrature must be considered at every interval between breakpoints to account for the discontinuous nature of the parametrization. Numerical experiments reveal that Gauss-Legendre quadratures are a competitive choice in front of other quadrature rules such as trapezoidal and Simpson composite rules or Romberg's integration, see [32] for a detailed analysis.

The NEFEM also requires to compute integrals over an element Ω_e with one side Γ_e on the NURBS boundary, see Figure 2, that is

$$\int_{\Omega_e} f \, dx \, dy = |J_{\boldsymbol{\Psi}}| \int_{I_e} f \, d\xi \, d\eta \tag{8}$$
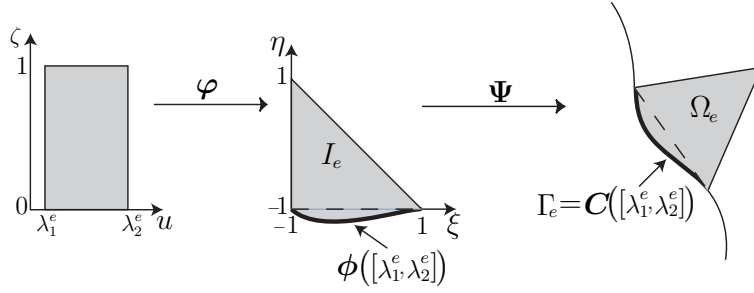
Figure 4. Transformation from $[\lambda_1^e, \lambda_2^e] \times [0, 1]$ to I_e and Ω_e

where $|J_{\mathbf{\Psi}}|$ is the determinant of the Jacobian of the linear transformation $\mathbf{\Psi}$. The computation

of (8) requires a numerical quadrature for every curved element I_e. Reference [32] presents

different alternatives and discusses their advantages and disadvantages. It is shown that

the best alternative corresponds to the definition of a transformation from the rectangle

$[\lambda_1^e, \lambda_2^e] \times [0, 1]$ to the curved element I_e, see Figure 4. That is, under the non restrictive

assumption that nodes are numbered following Remark 1,

$$\boldsymbol{\varphi} \; : [\lambda_1^e, \lambda_2^e] \times [0, 1] \longrightarrow I_e$$

$$(\lambda, \zeta) \longmapsto \left\{ \begin{array}{c} \varphi_1 \\ \varphi_2 \end{array} \right\} := \left\{ \begin{array}{c} \phi_1(\lambda)(1 - \zeta) - \zeta \\ \phi_2(\lambda)(1 - \zeta) + \zeta \end{array} \right\} \tag{9}$$

where $\boldsymbol{\phi} = (\phi_1, \phi_2)^T := \mathbf{\Psi}^{-1} \circ \boldsymbol{C}$ is the parametrization of the trimmed NURBS corresponding

to the curved side in I_e. Note that such a parametrization is linear in ζ and as discussed in [6]

this induces some important practical advantages.

Thus, using the transformations shown in Figure 4, integral (8) is computed as

$$\int_{\Omega_e} f \, dx \, dy = |J_{\mathbf{\Psi}}| \int_{I_e} f \, d\xi \, d\eta \simeq |J_{\mathbf{\Psi}}| \sum_{i=1}^{\mathtt{n_{ip}}} \sum_{j=1}^{\mathtt{m_{ip}}} f(\boldsymbol{\xi}_{ij}) |J_{\boldsymbol{\varphi}}(\lambda_i, \zeta_j)| \, \omega_i \varpi_j \tag{10}$$

where $\mathtt{n_{ip}}$ and $\mathtt{m_{ip}}$ are the number of integration points in the λ and ζ directions, respectively,

Copyright © 2007 John Wiley & Sons, Ltd.

Int. J. Numer. Meth. Fluids 2007; **00**:1–28

Prepared using fldauth.cls

$\boldsymbol{\xi}_{ij} := \boldsymbol{\varphi}(\lambda_i, \zeta_j)$, $\{\lambda_i, \omega_i\}$ and $\{\omega_i, \varpi_i\}$ are the 1D quadrature points and weights for $[\lambda_1^e, \lambda_2^e]$ and $[0, 1]$ respectively, and $|J_{\boldsymbol{\varphi}}|$ is the determinant of the Jacobian of the transformation $\boldsymbol{\varphi}$.

5. NUMERICAL RESULTS

To evaluate the accuracy and the efficiency of the proposed methodology, a classical inviscid test case is considered: the subsonic flow around a circle at free-stream Mach number $M_\infty = 0.3$. In all the numerical computations a DG formulation is adopted. As first studied in [1] and later in [2, 5, 33], DG discretization of the wall boundary condition is very sensitive to the geometrical description of curved boundaries. More precisely, in [1] the authors show that it is not possible to converge to the correct physical solution if the computational boundary is approximated with piecewise linear polynomials. When the steady state is reached the solution is advanced in time until the density residual is reduced to 10^{-10} in the $\mathcal{L}^2(\Omega)$ norm.

The behavior of the proposed method for both linear and high order interpolations is studied in the following sections.

5.1. Low order computations

Four O-meshes with 16×4, 32×8, 64×16, and 128×32 nodes, and 128, 512, 2048 and 8192 elements respectively, are considered for low order computations. A detailed view of these meshes near the circle is represented in Figure 5, see [5] for the mesh generation details.

Figure 6 shows Mach number isolines for isoparametric FE with linear interpolation. The results corroborate the conclusions first published by Bassi and Rebay [1] in the context of DG methods. Even if the mesh is highly refined near the circle, for instance using the fine mesh of figure 5 with 128 curved elements along the circular boundary, a non-physical entropy

(a) 16×4 (b) 32×8

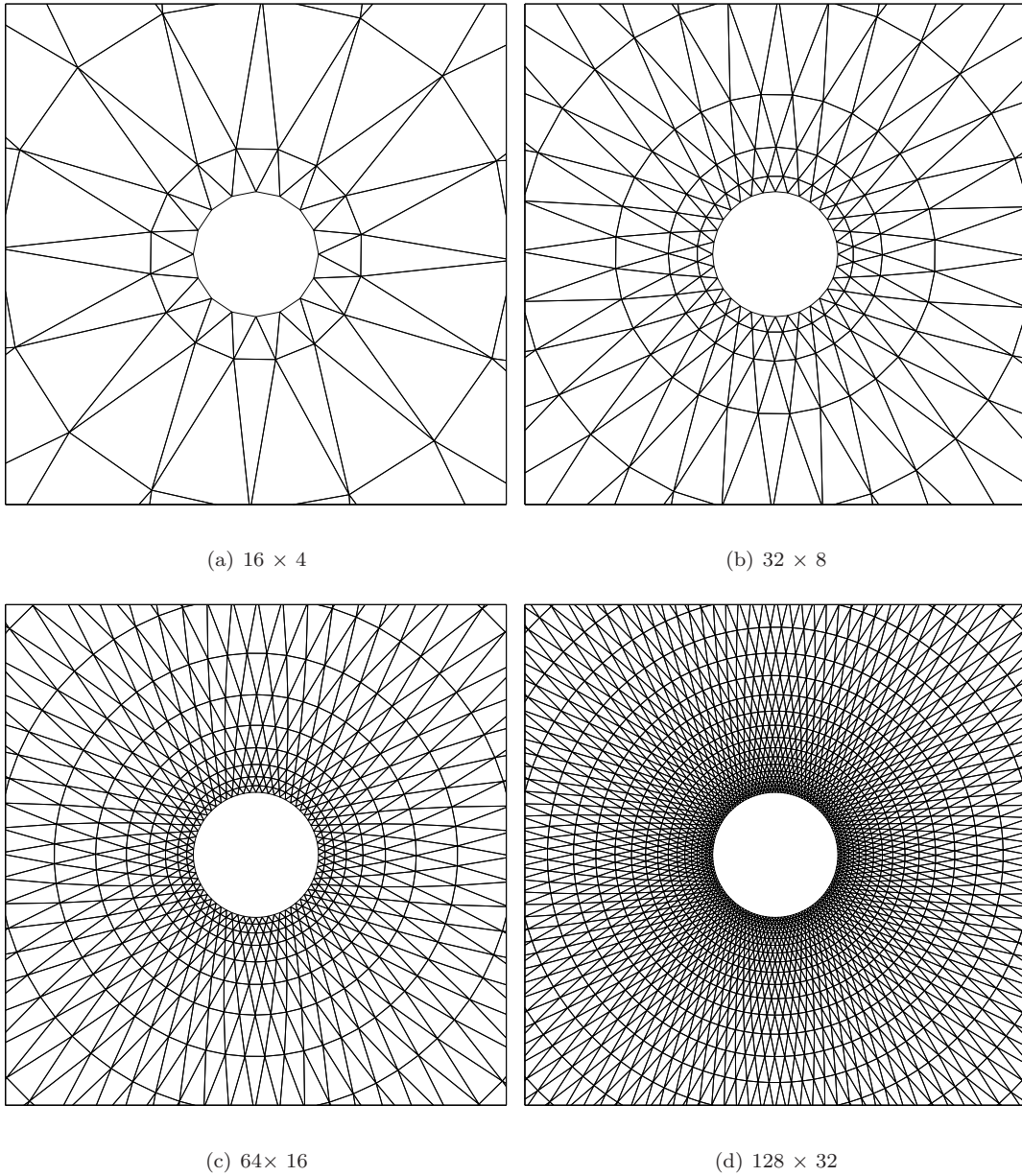(c) 64×16 (d) 128×32

Figure 5. Detail of O-meshes for low order computations

production is observed behind the wall. As it is commented in [34], the singularities of the polygonal approximation of the boundary generate entropy and the solution develops a non-

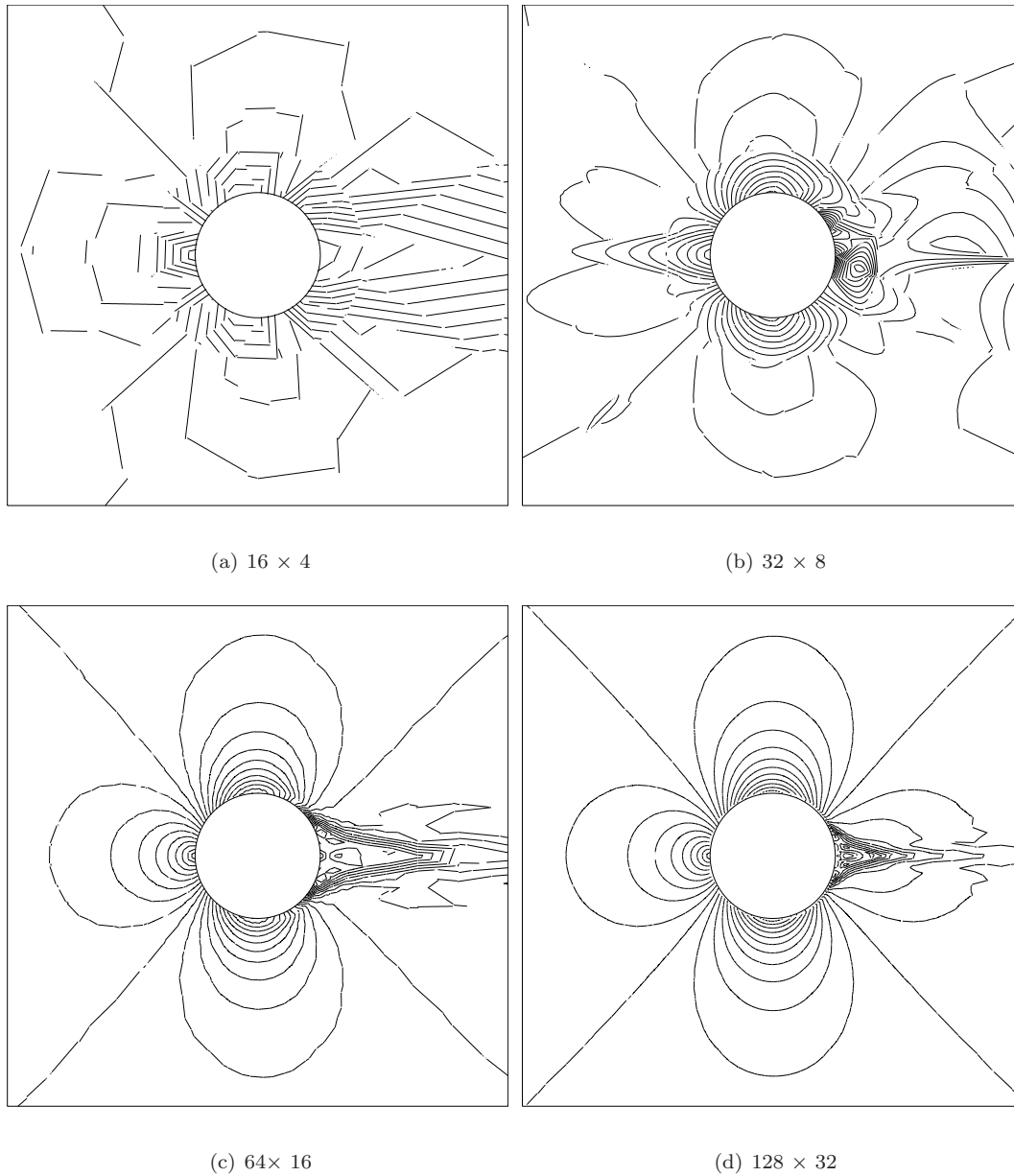physical wake that makes impossible the convergence to the correct solution.

(a) 16 × 4

(b) 32 × 8

(c) 64× 16

(d) 128 × 32

Figure 6. Mach number isolines with isoparametric FE and p=1

Figure 7 shows Mach number isolines computed with the NEFEM approach using linear

interpolation. The results reveal a major symmetry of the Mach number patterns, even if coarse meshes are used. Moreover, the NEFEM allows to converge to the correct physical solution using the fine mesh with a piecewise linear approximation of the solution. The exact computation of the outward unit normal improves the imposition of the solid wall boundary condition in such a way that the entropy production is clearly reduced with respect to the isoparametric FE solution.

$\mathcal{L}^2$ norm of entropy errors measured on the upper mid of the circle are reported in Table I. For isoparametric FE, the entropy production observable in Figure 6 deteriorates the h-convergence rate. In contrast, NEFEM exhibits the optimal convergence rate using linear interpolation. Results of Table I also show that, to achieve an entropy error of $6 \ 10^{-3}$ with isoparametric FE it is mandatory to perform the computation on the fine mesh, whereas the second mesh suffices to obtain the same precision with the NEFEM. Thus, the extra computational cost associated to the numerical integration of the NEFEM is clearly surpassed by the drastic saving in number of degrees of freedom (ten times less degrees of freedom).

Figure 8 shows pressure loss and pressure coefficient distributions on the upper mid of the circle. At the most critical point, the stagnation point behind the circle, the maximum pressure loss error with isoparametric FE in the fine mesh is $2.3 \ 10^{-2}$, whereas the NEFEM maximum error is reduced more than one order of magnitude, that is 10^{-3}. Moreover, in the fine mesh, the pressure coefficient error at the stagnation point is 0.4 for standard FE and $6 \ 10^{-3}$ for NEFEM, almost two order of magnitude more precise for the same number of degrees of freedom.

To conclude, it is important to recall that the problematic associated to the solid wall boundary condition is not an exclusive matter of DG methods. In [8] the same problem had
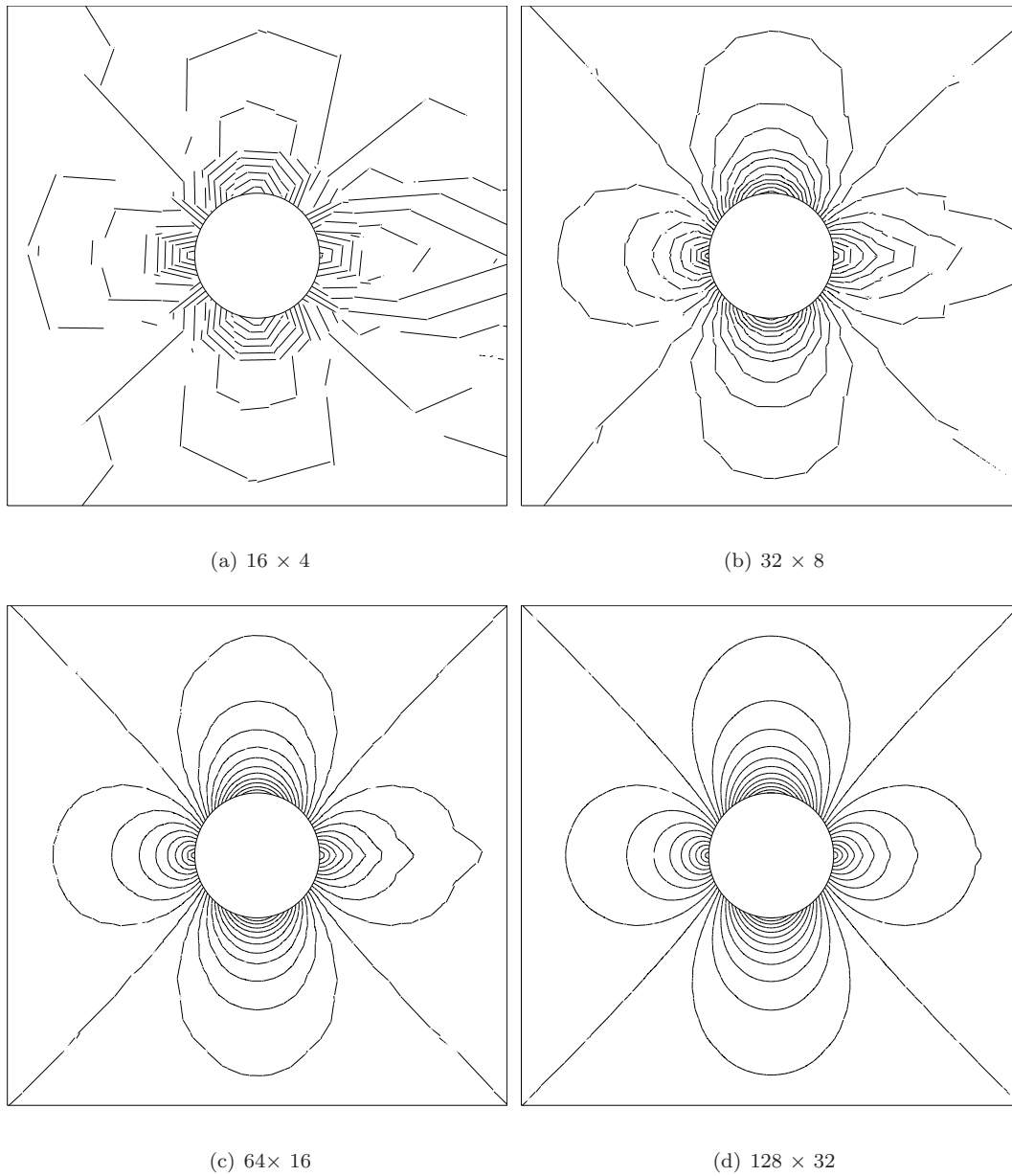
(a) 16 × 4

(b) 32 × 8

(c) 64× 16

(d) 128 × 32

Figure 7. Mach number isolines with NEFEM and p=1

been observed by Barth in the FV framework. Thus, the benefits of the NURBS-Enhanced
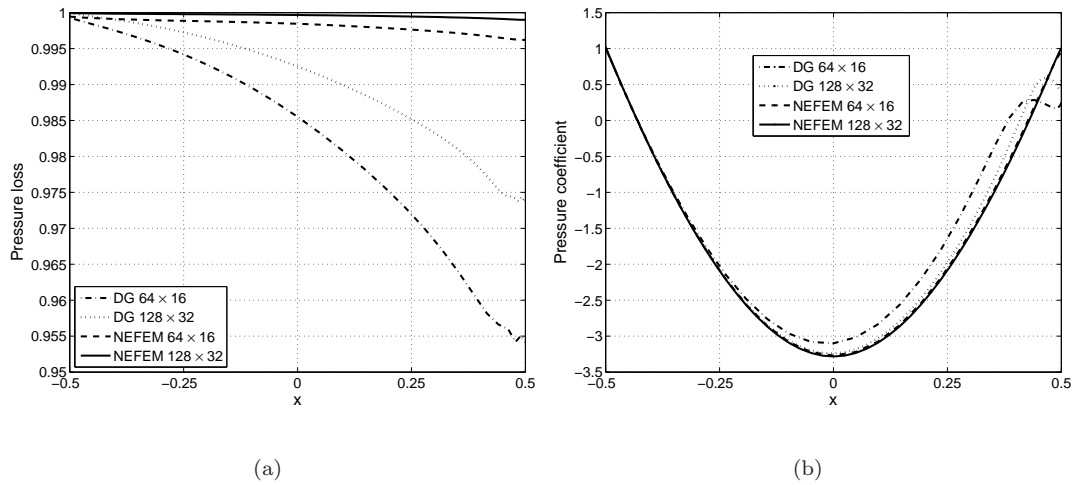
concept are extensible to FV methods.

Figure 8. (a) Pressure loss distribution and (b) pressure coefficient distribution, at the upper mid of

the circle for $p=1$

Finally, a comparison between h and p-refinement strategies for the NEFEM is presented in order to recall the superiority of high order interpolations, see [35, 36] for classical FE and [6] for the NEFEM. For the p-refinement strategy the coarser mesh in Figure 5 is considered with an interpolation degree $p = 1, 2, 4, 6$. Figure 9 shows the logarithm of the $\mathcal{L}^2$ entropy error in the upper mid of the circle as a function of the logarithm of the number of degrees of freedom. Although the h-refinement process shows the optimal rate of convergence (straight line with slope $p/2$), it is clearly surpassed by the exponential decay of the error for the p-refinement strategy. Thus, the advantage of using high order interpolations is clear, specially in the context of a DG formulation.

The performance of the NEFEM for high order computations is studied next.
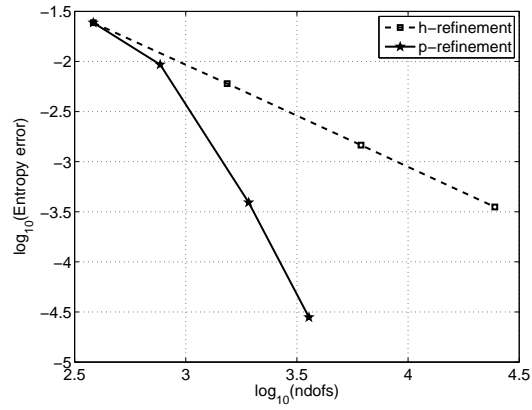
Figure 9. $\mathcal{L}^2$ entropy error at the upper mid of the circle for h and p-refinement using NEFEM

5.2. High order computations

Following [34], for high order computations outer boundaries are placed near the obstacle, and the symmetry with respect to the x axis is used in order to reduce the number degrees of freedom. Two computational meshes, represented in Figure 10, are considered. The coarser mesh has 26 elements and only 2 curved elements to describe a half of a circle, and the fine mesh is obtained by uniform refinement.

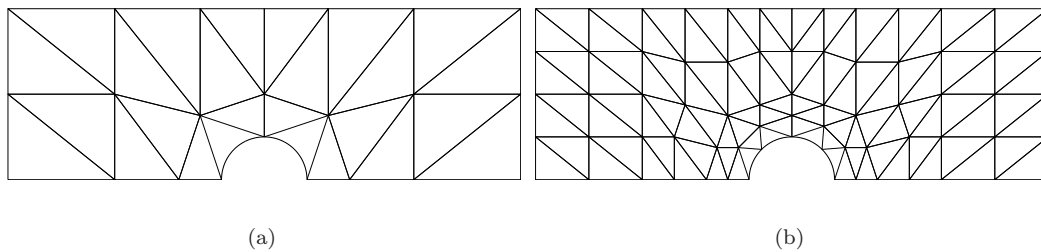(a)   (b)

Figure 10. Computational meshes for high order computations

Figures 11 and 12 show Mach number isolines in the coarser mesh of Figure 10 using

isoparametric FE and the NEFEM, respectively. For both methods, a degree of interpolation $p=2$ or $p=4$ is not sufficient to properly capture the solution, and the entropy production behind the circle is clearly observed. For higher degree of interpolation, namely for $p=6$ and $p=8$, the isoparametric FE solution displays an slight asymmetry with respecto to the y axis due to the spurious entropy production. For the NEFEM, using an interpolation degree $p=6$ the solution exhibits better symmetry than using isoparametric FE with $p=8$, and, for the NEFEM with $p=8$ a visually symmetric Mach number distribution is obtained.

(a) $p=2$ (b) $p=4$

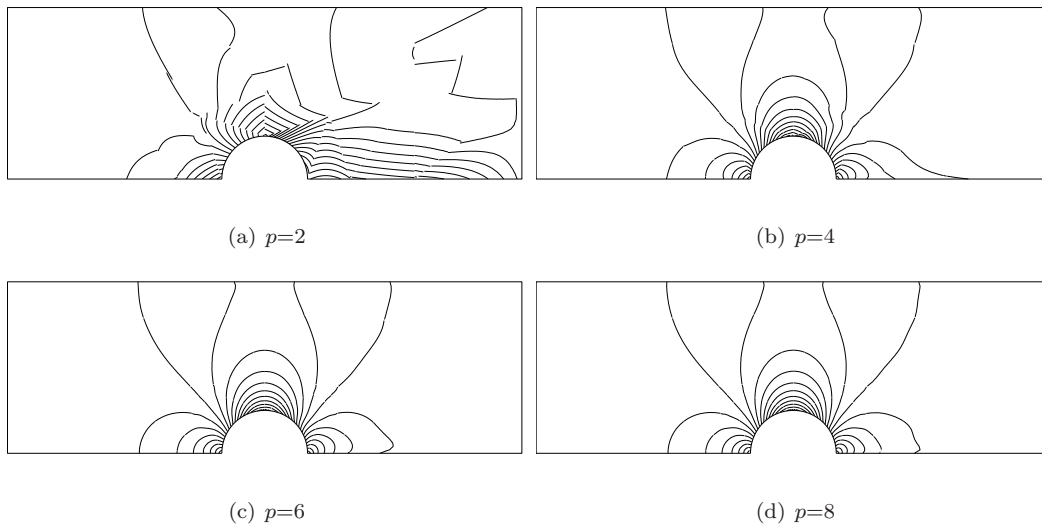(c) $p=6$ (d) $p=8$

Figure 11. Mach number isolines for isoparametric FE in the coarse mesh

Figures 13 and 14 show Mach number isolines for the fine mesh in Figure 10 using isoparametric FE and the NEFEM, respectively. Again, for both methods, quadratic elements are insufficient to properly capture the solution. For high order of interpolation, say $p=4$, isoparametric FE solution shows a slight asymmetry with respect to the y axis, and a degree of interpolation $p=6$ is mandatory to obtain a visually symmetric Mach number distribution. For the NEFEM, a degree of interpolation $p=4$ is sufficient to reduce the non-physical entropy
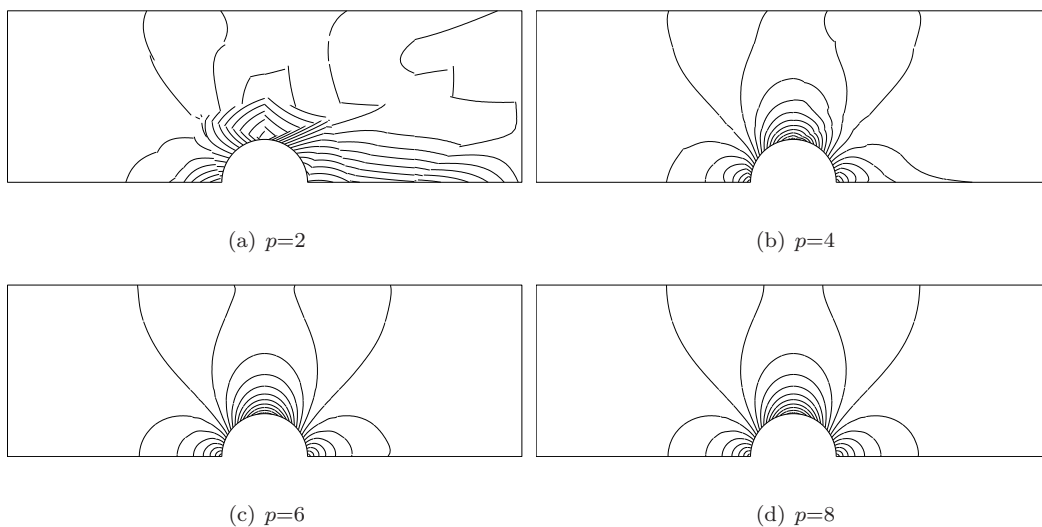
(a) p=2   (b) p=4

(c) p=6   (d) p=8

Figure 12. Mach number isolines for NEFEM in the coarse mesh

production in such a way that the Mach number pattern is visually symmetric.

(a) p=2   (b) p=4

(c) p=6   (d) p=8
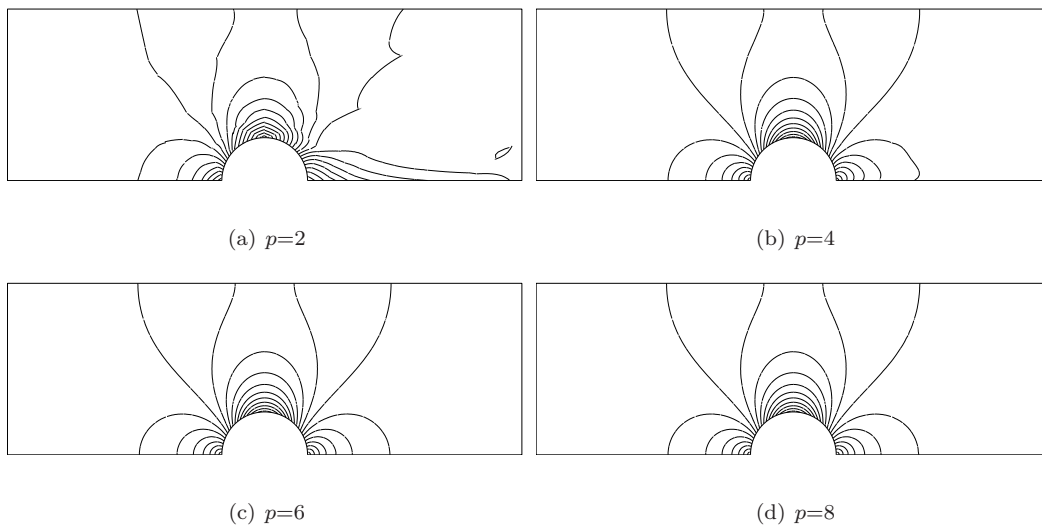
Figure 13. Mach number isolines for isoparametric FE in the fine mesh

The accuracy in terms of the entropy error for high order computations is analyzed next.

(a) $p=2$ (b) $p=4$
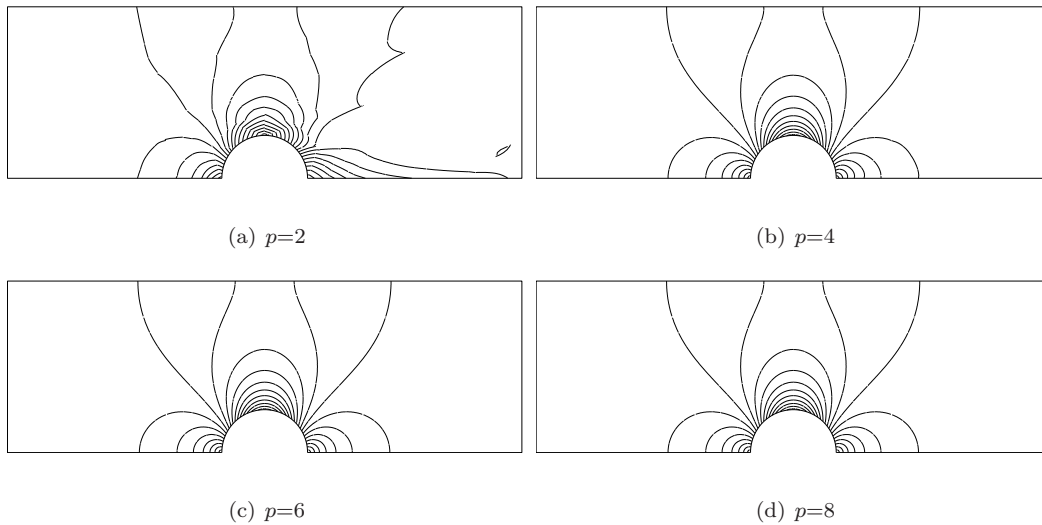
(c) $p=6$ (d) $p=8$

Figure 14. Mach number isolines for NEFEM in the fine mesh

Figure 15 shows the $\mathcal{L}^2$ the entropy error at the upper mid of the circle as a function of the square root of the number of degrees of freedom for isoparametric FE and for the NEFEM. The p-convergence for isoparametric FE computations is clearly deteriorated for high order
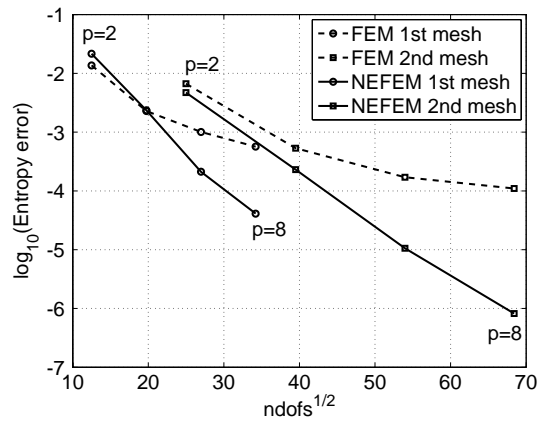

Figure 15. Entropy error on the circle surface (Γ^c) for p-refinement

interpolations, whereas the NEFEM maintains the exponential p-convergence, as stated in [6]. The results reveal that the best accuracy that can be obtained with isoparametric FE on the coarser mesh corresponds to an error of $5 \ 10^{-4}$. In order to improve the accuracy of the isoparametric FE computation, an hp-refinement strategy must be adopted. For instance, an error down to 10^{-4} can be achieved with the second mesh shown in Figure 10. For the NEFEM, if the first mesh is considered, the error with p=8 is $4 \ 10^{-5}$, more than one order of magnitude more precise than using isoparametric FE with the same number of degrees of freedom. Moreover, if the second mesh is considered, the NEFEM error with p=8 is 10^{-6}, two orders of magnitude more precise than standard isoparametric FE. It is also worth noting that with a high-order approximation of degree p=8, similar accuracy is obtained using isoparametric FE in the fine mesh and NEFEM in the coarse mesh, that is NEFEM requires four times less degrees of freedom.

Finally, it is important to recall that in a FE adaptive process, see [37], the computational mesh must be locally refined to properly capture both the solution and the geometry, whereas in a NEFEM context the adaptive process is controlled only by the complexity of the solution, independently of the geometrical complexity of the domain, and therefore reducing the necessary number of degrees of freedom to achieve a desired accuracy.

6. CONCLUDING REMARKS

The NEFEM combined with a DG formulation is proposed for the numerical solution of the compressible Euler equations. A classical test for inviscid flow solvers is considered to evaluate the accuracy and the efficiency of the proposed methodology in front of isoparametric FE. The proper imposition of the wall boundary condition in the NEFEM allows accurate

computations even with a linear interpolation of the solution. With isoparametric linear elements it is not possible to converge to the correct solution using linear interpolation, even if the mesh is drastically refined near curved boundaries. Moreover, under p-refinement, the optimal (exponential) convergence is achieved with NEFEM and not for isoparametric FE.

Numerical results demonstrate that the NEFEM is a powerful method for the solution of the Euler equations of gas dynamics, more efficient than classical isoparametric FE. The extra cost of the NEFEM, due to the numerical integration over elements along the NURBS boundary, is surpassed by the important saving in number of degrees of freedom. More precisely, NEFEM provides similar accuracy than isoparametric FE using between 4 and 10 times less degrees of freedom.

REFERENCES

1. F. Bassi and S. Rebay, "High-order accurate discontinuous finite element solution of the 2D Euler equations," *J. Comput. Phys.*, vol. 138, no. 2, pp. 251–285, 1997.

2. H. van der Ven and J. J. W. van der Vegt, "Space-time Discontinuous Galerkin finite element method with dynamic grid motion for inviscid compressible flows: II. Efficient flux quadrature," *Comput. Methods Appl. Mech. Eng.*, vol. 191, no. 41-42, pp. 4747–4780, 2002.

3. D. Xue and L. Demkowicz, "Control of geometry induced error in hp finite element (FE) simulations. I. Evaluation of FE error for curvilinear geometries," *Int. J. Numer. Anal. Model.*, vol. 2, pp. 283–300, 2005.

4. T. J. R. Hughes, J. A. Cottrell, and Y. Bazilevs, "Isogeometric analysis: CAD, finite elements, NURBS, exact geometry and mesh refinement," *Comput. Methods Appl. Mech. Eng.*, vol. 194, no. 39–41, pp. 4135–4195, 2005.

5. L. Krivodonova and M. Berger, "High-order accurate implementation of solid wall boundary conditions in curved geometries," *J. Comput. Phys.*, vol. 211, no. 2, pp. 492–512, 2006.

6. R. Sevilla, S. Fernández-Méndez, and A. Huerta, "NURBS-Enhanced Finite Element Method (NEFEM)," 2007. Submitted.

7. A. Dadone and B. Grossman, "Surface boundary conditions for the numerical solution of the Euler equations.," *AIAA Journal*, vol. 32, no. 2, pp. 285–293, 1994.

8. T. Barth, *Simplified numerical methods for gas dynamics systems on triangulated domains*. PhD thesis, Department of Aeronautics and Astronautics, Stanford University, 1998.

9. Z. J. Wang and Y. Sun, "A curvature-based wall boundary condition for the Euler equations on unstructured grids," in *Proceedings of the 40th AIAA Aerospace Sciences Meeting and Exhibit*, (Nevada), AIAA, 2002.

10. Z. J. Wang and Y. Liu, "Extension of the spectral volume method to high-order boundary representation," *J. Comput. Phys.*, vol. 211, pp. 154–178, 2006.

11. L. Piegl and W. Tiller, *The NURBS Book*. London: Springer-Verlag, 1995.

12. F. Cirak, M. Ortiz, and P. Schröder, "Subdivision surfaces: A new paradigm for thin-shell finite-element analysis," *Int. J. Numer. Meth. Engrg.*, vol. 47, no. 12, pp. 2039–2072, 2000.

13. J. Donea and A. Huerta, *Finite Element Methods for Flow Problems*. Chichester: John Wiley & Sons, 2002.

14. J. D. Anderson, *Modern Compressible Flow: with Historical Perspective*. New York: McGraw-Hill, 1982.

15. C. Hirsch, *Numerical Computation of Internal and External Flows. Volume 2: Computational methods for insviscid and viscous flows*. Chichester: John Wiley & Sons, 1988.

16. C. B. Laney, *Computational gasdynamics*. Cambridge: Cambridge University Press, 1998.

17. B. Cockburn, *Discontinuous Galerkin methods for Computational Fluid Dynamics*, vol. 3 of *Encyclopedia of Computational Mechanics*, ch. 4. Wiley, 2004.

18. E. F. Toro, *Riemann solvers and numerical methods for fluid dynamics*. Berlin: Springer, second ed., 1997.

19. B. Cockburn and C. W. Shu, "The Runge-Kutta Discontinuous Galerkin method for conservation laws. V. Multidimensional systems," *J. Comput. Phys.*, vol. 141, no. 2, pp. 199–224, 1998.

20. R. Leveque, *Finite Volume Methods for Hyperbolic Problems*. Cambridge: Cambridge University Press, 2002.

21. D. Kuzmin and M. Möller, "Algebraic flux correction II. Compressible Euler equations," in *Flux-corrected Transport: Principles, Algorithms, And Applications*, Springer Verlag, 2005.

22. B. Cockburn and C. W. Shu, "TVB Runge-Kutta local projection Discontinuous Galerkin finite-element method for conservation-laws. II. General framework," *Math. Comp.*, vol. 52, no. 186, pp. 411–435, 1989.

23. V. Dolejsí and M. Feistauer, "A semi-implicit Discontinuous Galerkin finite element method for the

numerical solution of inviscid compressible flow," *J. Comput. Phys.*, vol. 198, no. 2, pp. 727–746, 2004.

24. P. Persson and J. Peraire, "An efficient low memory implicit DG algorithm for time dependent problems," in *Proceedings of the 44th AIAA Aerospace Sciences Meeting and Exhibit*, (Nevada), AIAA, 2006.

25. S. Gottlieb and C. W. Shu, "Total variation diminishing Runge-Kutta schemes," *Math. Comp.*, vol. 67, no. 221, pp. 73–85, 1998.

26. H. L. Atkins and C. W. Shu, "Quadrature-free implementation of Discontinuous Galerkin method for hyperbolic equations," *AIAA Journal*, vol. 36, no. 5, pp. 775–782, 1998.

27. P. G. Koen Hillewaert, Nicolas Chevaugeon and J.-F. Remacle, "Hierarchic multigrid iteration strategy for the Discontinuous Galerkin solution of the steady Euler equations," *Internat. J. Numer. Methods Fluids*, vol. 51, pp. 1157–1176, 2006.

28. J. S. Hesthaven and T. Warburton, "Nodal high-order methods on unstructured grids. I. Time-domain solution of Maxwell's equations," *J. Comput. Phys.*, vol. 181, no. 1, pp. 186–221, 2002.

29. Q. Chen and I. Babuška, "Approximate optimal points for polynomial interpolation of real functions in an interval and in a triangle," *Comput. Methods Appl. Mech. Eng.*, vol. 128, no. 3–4, pp. 405–417, 1995.

30. Q. Chen and I. Babuška, "The optimal symmetrical points for polynomial interpolation of real functions in the tetrahedron," *Comput. Methods Appl. Mech. Eng.*, vol. 137, pp. 89–94, 1996.

31. M. A. Taylor, B. A. Wingate, and R. E. Vincent, "An algorithm for computing Fekete points in the triangle," *SIAM J. Numer. Anal.*, vol. 38, no. 5, pp. 1707–1720, 2000.

32. R. Sevilla and S. Fernández-Méndez, "Numerical integration for the 2D NURBS-Enhanced Finite Element Method," 2007. Submitted.

33. H. Luo, J. D. Baum, and R. Löhner, "A fast, p-multigrid Discontinuous Galerkin method for compressible flows at all speeds," in *Proceedings of the 44th AIAA Aerospace Sciences Meeting and Exhibit*, (Nevada), AIAA, 2006.

34. B. Cockburn, G. E. Karniadakis, and C. W. Shu, "The development of Discontinuous Galerkin methods," in *Discontinuous Galerkin Methods* (B. Cockburn, G. E. Karniadakis, and C.-W. Shu, eds.), vol. 11 of *Lecture Notes in Computational Science and Engineering*, pp. 3–50, Berlin: Springer-Verlag, 2000.

35. B. Szabó and I. Babuška, *Finite Element Analysis*. New York: John Wiley & Sons, 1991.

36. B. Szabó, A. Düster, and E. Rank, *The p-version of the Finite Element Method*, vol. 1 of *Encyclopedia of Computational Mechanics*, ch. 5. Wiley, 2004.

37. A. Huerta, A. Rodríguez-Ferran, P. Díez, and J. Sarrate, "Adaptive finite element strategies based on error assessment," *Int. J. Numer. Meth. Engrg.*, vol. 46, pp. 1803–1818, 1999.

Mesh	FEM		NEFEM	
	ϵ_{ent}	r	ϵ_{ent}	r
16×4	5.74E-02	-	2.43E-02	-
32×8	2.34E-02	1.30	6.01E-03	2.03
64×16	1.40E-02	0.73	1.46E-03	2.04
128×32	6.53E-03	1.10	3.53E-04	2.05

Table I. $\mathcal{L}^2$ entropy error at the upper mid of the circle and rate of convergence (r) for p=1